

DECT-based Space-Squeeze Method for Multi-Class Classification of Metastatic Lymph Nodes in Breast Cancer

Hai Jiang^{†,1}, Chushan Zheng^{†,3}, Jiawei Pan¹, Yuanpin Zhou⁴,

Qiongtong Liu⁵, Xiang Zhang^{*,2}, Jun Shen^{*,2}, Yao Lu^{*,1}

¹School of Computer Science and Engineering, Sun Yat-sen University, P.R. China

²Department of Radiology, Sun Yat-Sen Memorial Hospital, Sun Yat-Sen University, P.R. China

³Medical Imaging Center, Shenzhen Hospital of Southern Medical University, P.R. China

⁴Hithink RoyalFlush Information Network Co., Ltd., Hangzhou, P.R. China

⁵Department of Radiology, The third Affiliated Hospital of Guangzhou Medical University, P.R. China

Version typeset June 11, 2025

[†] Equal contribution

* Correspondence

email: luyao23@mail.sysu.edu.cn, shenjun@mail.sysu.edu.cn,
zhangx345@mail.sysu.edu.cn

Abstract

Background: Accurate assessment of metastatic burden in axillary lymph nodes is crucial for guiding breast cancer treatment decisions, yet conventional imaging modalities struggle to differentiate metastatic burden levels and capture comprehensive lymph node characteristics. This study leverages dual-energy computed tomography (DECT) to exploit spectral-spatial information for improved multi-class classification.

Purpose: To develop a noninvasive DECT-based model classifying sentinel lymph nodes into three categories: no metastasis (N_0), low metastatic burden ($N_{+(1-2)}$), and heavy metastatic burden ($N_{+(\geq 3)}$), thereby aiding therapeutic planning.

Methods: We propose a novel space-squeeze method combining two innovations: (1) a channel-wise attention mechanism to compress and recalibrate spectral-spatial features across 11 energy levels, and (2) virtual class injection to sharpen inter-class boundaries and compact intra-class variations in the representation space.

Results: Evaluated on 227 biopsy-confirmed cases, our method achieved an average test AUC of 0.86 (95% CI: 0.80-0.91) across three cross-validation folds, outperforming established CNNs (VGG, ResNet, etc). The channel-wise attention and virtual class components individually improved AUC by 5.01% and 5.87%, respectively, demonstrating complementary benefits.

Conclusions: The proposed framework enhances diagnostic AUC by effectively integrating DECT’s spectral-spatial data and mitigating class ambiguity, offering a promising tool for noninvasive metastatic burden assessment in clinical practice.

Contents

I. Introduction **1**

II. Materials and Methods **4**

 II.A. Data 4

 II.B. Architecture of the CNN-Based Classification Pipeline 5

 II.B.1. Feature space squeezing 7

 II.B.2. Representation space squeezing 8

 II.C. Experimental Configuration and Training Protocols . 9

III. Results **11**

 III.A. Ablation Study of Key Methodological Components . 11

 III.B. Impact of Single Energy-Level Inputs and Hidden
 Layer Optimization 12

 III.C. Comparative Analysis with Established CNN Archi-
 tectures 13

 III.D. ROC Curve Analysis and Statistical Validation 13

IV. Discussion **15**

V. Conclusions **18**

References **18**

I. Introduction

Breast cancer (BC) has been the most commonly diagnosed cancer worldwide from 2000 to 2022, surpassing Lung cancer in incidence (2.25 million BC cases vs. 2.21 million Lung cancer cases) ^{1,2,3}. The sentinel lymph node (SLN), the first node to drain the primary tumor, plays a critical role in treatment planning and determining the necessity of surgical intervention, potentially avoiding unnecessary biopsies ⁴. Based on nodal dissection pathology, SLN metastatic status is categorized as disease-free axilla (N_0), low metastatic burden ($N_{+(1-2)}$), or heavy metastatic burden ($N_{+(\geq 3)}$) ^{5,6}. For SLN-positive patients, axillary lymph node dissection (ALND) has been the standard procedure to evaluate axillary lymph node metastasis and manage regional nodes. However, ALND can lead to complications such as upper limb edema, neuropathic pain, and arm numbness, particularly in patients with low metastatic burden ⁷. Emerging evidence suggests that ALND may be avoidable for SLN-positive patients with $N_{+(1-2)}$ status ⁸. Therefore, accurately identifying ALN status is essential, serving as a key indicator for cancer staging and guiding therapeutic decisions for BC patients.

Ultrasound (US) and histopathology are widely used for diagnosis but offer limited accuracy and require large datasets, making them less effective in small-sample settings ^{9,10}. Similarly, MRI and PET have shown suboptimal performance compared to SLN biopsy ¹¹. Although CT is commonly used for staging or detecting metastases in advanced BC, its preoperative application, particularly in predicting SLN metastasis, remains limited, often due to clinician inexperience. In contrast, dual-energy computed tomography (DECT) is emerging as a promising complementary modality ¹². DECT combines spectral Hounsfield unit curves with spatial imaging, allowing for the assessment of both tissue composition and lymph node metastasis. Its ability to capture tissue absorption differences across energy lev-

fig1

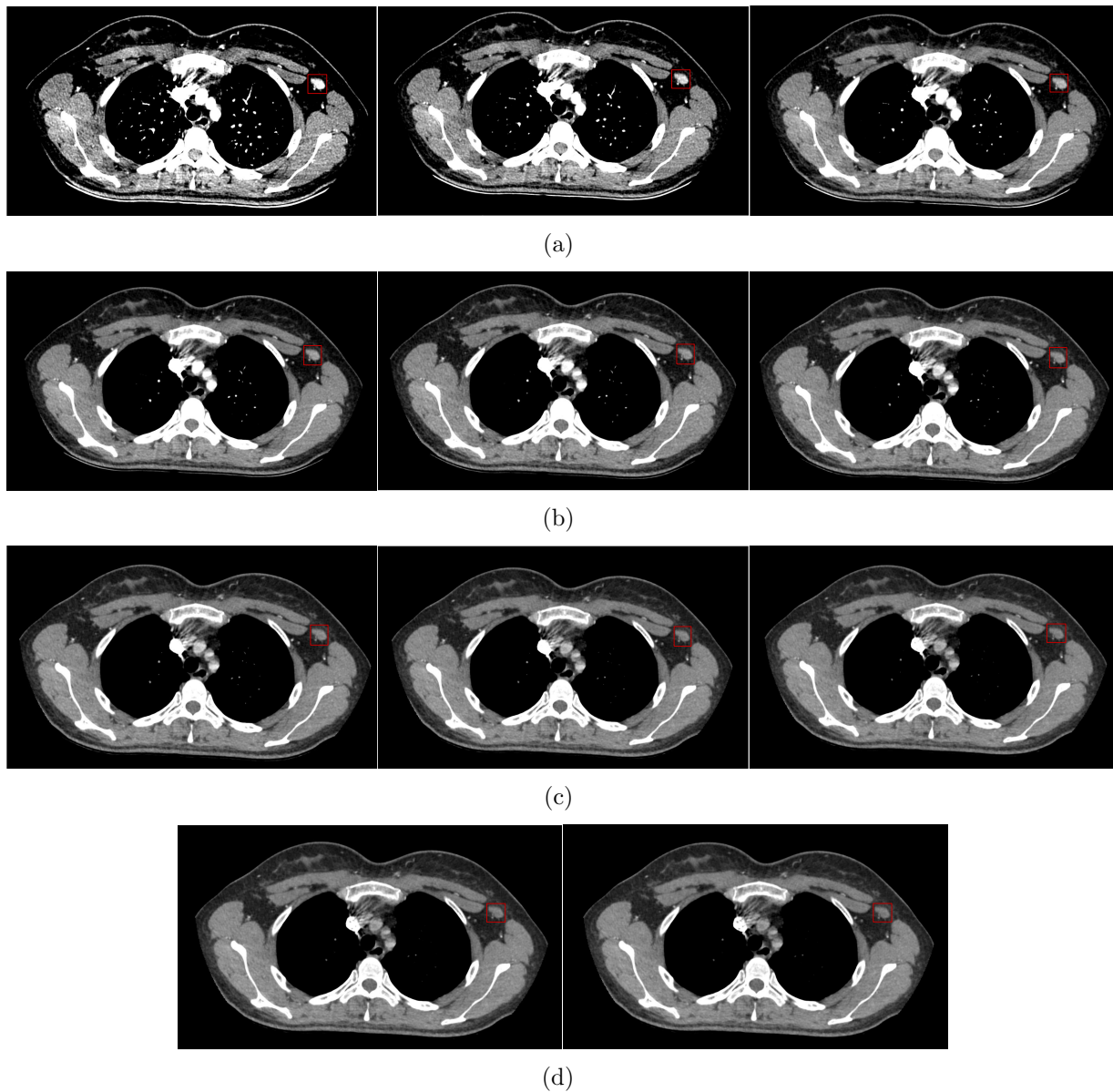


Figure 1: Subfigures (a) to (d) depict a patient with heavy-burden metastatic disease ($N_{+(\geq 3)}$) across 11 energy levels, ranging from 40 keV to 140 keV in 10 keV increments. The sentinel axillary lymph node is marked with a red bounding box.

els and provide high-resolution images enables a more comprehensive and detailed evaluation of lymph node characteristics in BC patients.

Existing methods mainly focus on detecting the presence or absence of sentinel ALN metastasis, typically classifying cases as N_0 and non- N_0 . For instance, Zhou et al. employed two deep learning models to predict ALN metastasis in BC patients ^{zhou2020lymph} [13], highlighting the potential of deep learning in this domain. Other studies using US data have applied statistical machine learning models for metastasis diagnosis ^{evans2014dogs, boughey2010cost, qiu2016nomogram} [14, 15, 16]. La Verde et al. used logistic regression to examine tumor and patient characteristics influencing SLN involvement in early-stage BC ^{la2016role} [17], while Tapia et al. applied logistic regression to pathological images, achieving an AUC of 0.74 ^{tapia2019predicting} [18]. In contrast, our study moves beyond binary classification by proposing a non-invasive, multi-class classification framework designed to support radiologists in making more accurate and comprehensive diagnoses.

Several challenges need to be addressed in this study:

- First, the use of a region of interest (RoI) that focuses on the largest sentinel ALN, combined with the limited dataset, increases the risk of overfitting in the deep CNN methods.
- Second, DECT's unique properties, which combine spectral information (Hounsfield unit curves) with spatial data across multiple energy levels, present the challenge of effectively extracting and utilizing both types of information.
- Third, sentinel ALNs exhibit variations across different energy levels, making it difficult for radiologists to discern discrepancies (Fig. ^{fig1} 1) in clinical scenarios. Capturing and leveraging the correlated information across these energy levels is therefore a significant challenge.
- Finally, the morphological similarities across different classes (Fig. ^{fig2} 6) increase the difficulty of classification, as the hidden

layers in CNNs tend to generate overlapping feature patterns that are challenging to control during training. Effectively managing these representations remains a critical challenge.

In this work, we propose a novel space-squeeze approach to address these issues. The manuscript is organized as follows: Section II introduces the materials, the proposed diagnostic model, and experimental setup. Section III presents the experimental results. Section IV provides an in-depth discussion of the findings. Finally, Section V gives the conclusions.

II. Materials and Methods

II.A. Data

dataset

Prior to this retrospective study, ethical approval was obtained from the Institutional Review Board at Sun Yat-sen Memorial Hospital, and written informed consent was secured from all patients. A total of 458 patients with histopathologically confirmed BC were initially recruited. All underwent chest and axillary spectral CT scans using a GE Discovery CT750HD scanner, with patients positioned supine. Dual-phasic contrast-enhanced imaging was performed using Iohexol (GE Healthcare, USA), injected at 4 *ml/s* via the ulnar vein with an automated injector (Medrad Stellant). Arterial-phase imaging employed semi-automatic contrast tracking. Of the 458 patients, 227 were included in the final analysis based on confirmed metastatic status. The remaining 231 were excluded for reasons such as prior therapy (47), pre-scan biopsy (105), benign lesions (74), micrometastasis (1), missing intraoperative biopsy (2), and data integrity issues (2). Among the included patients, 96 had confirmed metastasis (58 low burden, 38 heavy burden), while 131 were metastasis-free.

To evaluate model performance, the 227-patient dataset was split into training (151 cases) and test (76 cases) sets with stratification

by class labels. Training utilized 3-fold stratified cross-validation. Image pixel values were normalized using a background-aware formula where -2000 denoted background intensity and p_{min}^+ was the minimum non-background pixel value in the training fold. Model performance was assessed using the area under the receiver operating characteristic curve (AUC). Each patient’s data included 11 energy levels (40-140 keV in 10 keV intervals). An experienced radiologist (Xiang Zhang, 10 years in BC diagnosis, 5 years in segmentation) manually annotated the region of interest (RoI) along the largest lymph node contour on the largest axial slice. RoIs were cropped, resized to 176×176 pixels via bilinear interpolation, and centered for consistency.

II.B. Architecture of the CNN-Based Classification Pipeline

Building on the strengths of CNNs, our proposed method emphasizes efficiency through a shallow network architecture to minimize the risk of overfitting. As illustrated in Fig. [2](#)^{overview}, the model builds upon our previous work [49](#)^{zeng2021decoupling} and features four convolutional blocks (highlighted in yellow). The first block processes multi-channel input using a 1×1 kernel with a stride of 1, while the second and third blocks use 3×3 kernels with stride 2 to extract spectral and spatial features, respectively. This architecture, consisting of an embedding layer followed by three convolutional layers, is designed to decouple and integrate spectral and spatial information—effectively addressing the second challenge.

A feature-space squeezing module is integrated at the bottom-right of the first convolutional block, enhancing the model’s ability to refine learned features. Additionally, virtual class injection begins at the model’s input, with the corresponding injected fake label (depicted in red) incorporated into the model’s output.

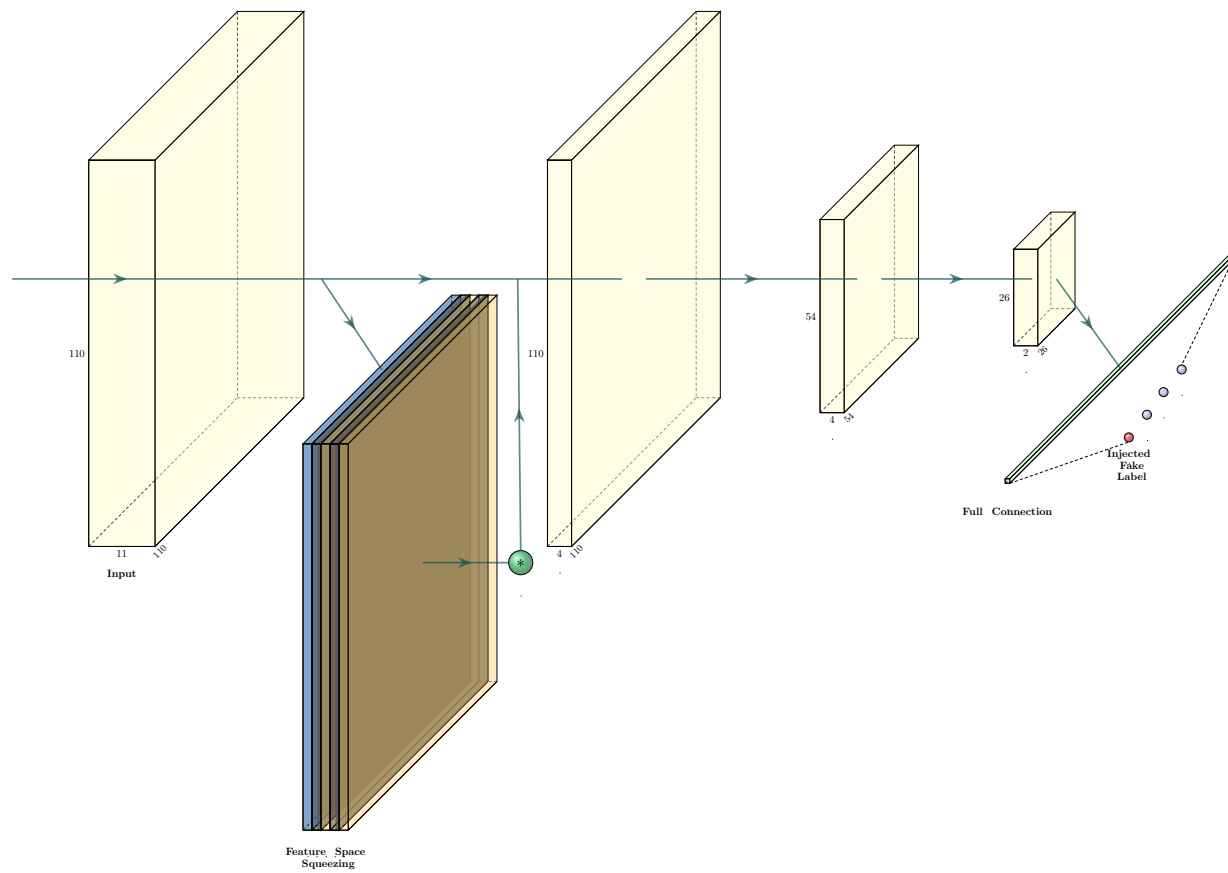
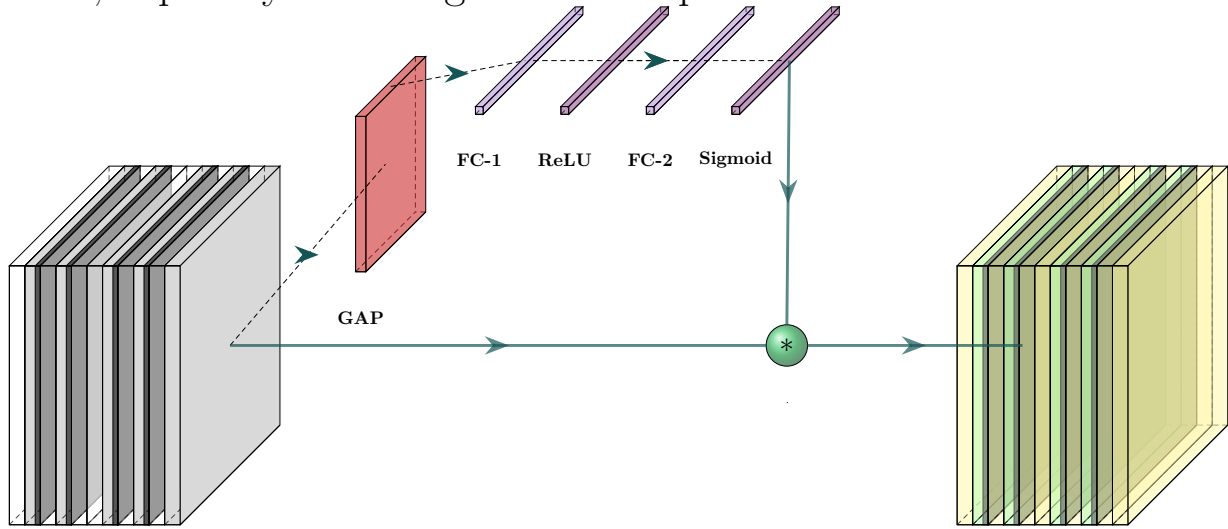


Figure 2: The proposed CNN-based framework.

II.B.1. Feature space squeezing

fss

To leverage the correlated information across the 11 selected energy levels, we compressed the feature map in the space encoded from images at all levels, and then re-excited it using learnable coefficients from an additional shallow embedding layer. By squeezing the feature space, our model aims to enhance its representational power, as the re-excitation process recalibrates features from different energy levels, explicitly modeling the interdependencies between them.



seblock

Figure 3: The detailed framework of feature-space-squeezing module.

We define the feature map in the feature space as $\mathbf{X} \in \mathbb{R}^{H \times W \times C}$, a 4D tensor where H , W and C denote height, width, and number of channels, respectively. The nonlinear mapping function \mathcal{T} , implemented via a **Squeeze-and-Excitation** (SE) block, transforms \mathbf{X} into $\mathbf{X}' \in \mathbb{R}^{H' \times W' \times C'}$ as $\mathbf{X}' = \mathcal{T}(\mathbf{X}) = \mathbf{X} \circledast \vec{w}$, where $\vec{w} \in \mathbb{R}^{C \times \frac{C}{r}}$ is a learnable coefficient vector and \circledast denotes the element-wise multiplication. Unlike pixel-wise averaging across energy levels, \vec{w} is generated through a compact embedding consisting of a Global Average Pooling (GAP) layer, followed by two Fully Connected (FC) layers with ReLU and Sigmoid activations. This structure captures channel-wise dependencies across the 11 energy levels. Specifically,

the GAP operation computes $\delta_k = \frac{1}{H \times W} \sum_{i=1}^H \sum_{j=1}^W x_k(i, j)$ for each feature map x_k , resulting in the vector $\vec{\delta} \in \mathbb{R}^C$. The excitation step then applies two FC layers with a reduction ratio r (chosen such that $\frac{C}{r} = 4$) to reduce and then restore the dimension:

$$\vec{\omega} = \mathbf{Sigmoid}(W_2 \cdot (\mathbf{ReLU}(W_1 \cdot \vec{\delta} + \vec{b}_1)) + \vec{b}_2), \quad (1)$$

where $W_1 \in \mathbb{R}^{\frac{C}{r} \times C}$, $W_2 \in \mathbb{R}^{C \times \frac{C}{r}}$, and $\vec{b}_i (i = 1, 2)$ are biases. The final output $\mathbf{X}' \in \mathbb{R}^{H' \times W' \times C'}$ incorporates both spatial and spectral context, enhancing representation of key energy-level features for downstream analysis.

rss

II.B.2. Representation space squeezing

The proposed classification CNN model encodes the 4-dimensional (4D) tensor for each patient into a high-dimensional representation space, which may contain thousands of patterns for recognition. By defining appropriate optimization loss functions, the model aims to identify the most relevant representative patterns for each class. However, since internal and external tumor lesions may share similar patterns across different classes, the boundaries between classes can become blurred, leading to confusion for the model. To address this, we squeeze the representation space by introducing virtual classes, which helps sharpen the inter-class boundaries and compact the intra-class regions (as shown in Fig. ^{VCvisual}4), thereby improving class discrimination.

We define the training dataset as $\{(x_i, y_i)\}$, where $x_i \in X$ represents the input features and $y_i \in Y = \{1, 2, \dots, C\}$ denotes the ground truth label. The angle between output feature vectors X_i and X_{i+1} is θ_i , and $\|\cdot\|$ denotes the L_2 norm. In standard classification, the softmax function normalizes model outputs, with the

VCvisual

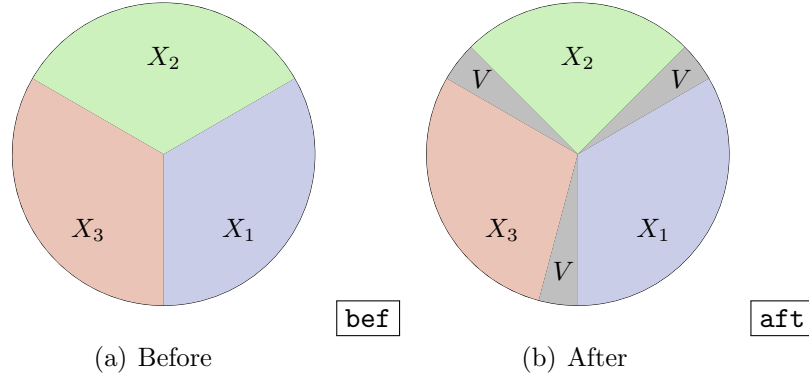


Figure 4: A simple 2D illustration showing the representation space before Fig. 4(a) and after Fig. 4(b) the injection of virtual class.

cross-entropy loss for class i defined as $l_i = -\log \frac{\exp(W_{y_i}^T X_i)}{\sum_{j=1}^C \exp(W_j^T X_i)}$, where W_j is the weight vector for class j . To enhance class separation, we introduce **virtual classes**, modifying the loss function to:

$$l'_i = -\log \frac{\exp(\|W_{y_i}\| \cdot \|X_i\| \cdot \cos \theta_{y_i})}{\sum_{j=1}^{C+V} \exp(\|W_j\| \cdot \|X_i\| \cdot \cos \theta_j)}, \quad (2)$$

and the overall loss becomes:

$$L' = \frac{1}{C} \sum_{i=1}^C l'_i. \quad (3)$$

This reformulation enlarges inter-class margins and compacts the decision boundaries by encouraging better angular separation, thereby improving classification performance.

II.C. Experimental Configuration and Training Protocols

Our framework was implemented on a platform equipped with an Intel(R) Xeon(R) CPU E5-2678 v3 @ 2.50 GHz and a single NVIDIA GeForce GTX 1080 Ti GPU (12 GB RAM), using *TensorFlow* 2.4.0 as the software environment. During training, we applied data augmentation techniques, including random flipping (*probability*=0.5)

and random rotation within a range of $\pm 18^\circ$ (*probability*=0.5), using the *Albumentations* library. The network was trained with an end-to-end approach, using a batch size of 32 and the *Adam* optimizer with a learning rate of 1×10^{-4} . To prevent overfitting, we applied L_2 regularization to the weights of each Conv2D kernel with a regularization parameter of 1×10^{-2} , and used the *Xavier* uniform method for kernel initialization. The training process spanned 500 epochs, with the training set stratified into three folds for cross-validation. Each input case was transformed into a $176 \times 176 \times 11$ tensor.

Since the dataset was collected from a single-center hospital (Sun Yat-sen Memorial Hospital), it was divided into training and test sets as detailed in Section [II.A.](#)^{dataset}. Due to the imbalanced class distribution and limited sample size, we employed three-fold stratified cross-validation using the *scikit-learn* library to ensure robust evaluation. Model performance was primarily measured using the micro-average area under the ROC curve (AUC) in a one-vs-rest (OvR) setting, with the highest validation AUC used for model checkpointing and final testing. To account for the dataset’s small size and imbalance, the test set AUC was further analyzed using the BCa method, which adjusts for bias and skewness in the bootstrap distribution to estimate the 95% confidence interval (CI) [efron1987better](#)²⁰.

To ensure fair evaluation of each component on this in-house dataset, the random seed was fixed at 42 across all experimental libraries, ensuring consistent parameter initialization, data augmentation, and data distribution (including training, validation, and testing) across all methods used in our experiments. Instead of the focal loss used in our previous work, we employed cross-entropy loss, enhanced by a virtual class mechanism as part of our representation space-squeezing strategy. To ensure comprehensive analysis, our feature-space-squeezing approach included a reduced coefficients layer, decreasing the number of coefficients from 11 to 4—an essen-

tial factor examined in our experiments. The implementation code is publicly available online ¹.

The 2-dimensional illustrations of the virtual class in Fig. ^{VCvisual}4 may create confusion regarding the number of injected virtual classes. However, as demonstrated in the previous study ^{chen2018virtual}24, the virtual class strategy is primarily implemented in the label space (conceptually). Therefore, even if multiple injected classes are shown, they can be considered as a single virtual class in the context of this approach.

III. Results

III.A. Ablation Study of Key Methodological Components

Building on our previous findings, we further evaluated the proposed method by analyzing each of its key components individually. In addition to the AUC scores obtained from the test set, we calculated the 95% confidence intervals using the BCa method for a more robust assessment.

Table 1: Ablation study of two components.

SE-Block	Virtual-Class	Test AUC - BCa 95% CI			Averaged AUC
		Fold-1	Fold-2	Fold-3	
×	×	0.7990 [0.7042, 0.8725]	0.7566 [0.6565, 0.8382]	0.7400 [0.6451, 0.8231]	0.7652
✓	×	0.8093 [0.7121, 0.8733]	0.8077 [0.6243, 0.8067]	0.7655 [0.6638, 0.8288]	0.8153
×	✓	0.8140 [0.7614, 0.8624]	0.8288 [0.7675, 0.8787]	0.8289 [0.7630, 0.8809]	0.8239
✓	✓	0.8528 [0.7978, 0.9003]	0.8861 [0.8263, 0.9322]	0.8582 [0.8043, 0.9127]	0.8657

Table ^{tab1}1 summarizes the results. The first row presents the base-line model without modifications, where spectral and spatial features are fully extracted and combined. The second row adds the SE-block, while the third introduces the virtual class. The final row represents

¹<https://github.com/pigejianghai/projects/tree/master/DECT/tfversion>

our full proposed method. Incorporating channel-wise attention increased the average AUC from 0.7652 to 0.8153. The virtual class injection boosted the baseline averaged AUC to 0.8239. Our complete method achieved the highest AUC of 0.8657, confirming the complementary effectiveness of both components in enhancing model performance.

III.B. Impact of Single Energy-Level Inputs and Hidden Layer Optimization

In the second ablation study, we assessed model performance using a single energy level as input. Since the SE-block requires multi-level input, only the effect of virtual class injection was evaluated. AUC results showed minimal variation across the eleven energy levels (0.77 ± 0.0015), underscoring the diagnostic limitations of single-energy inputs. Hence, we selected 40 keV as the representative level to demonstrate the impact of virtual class. Without virtual class injection, the model achieved an average AUC of 0.77 across folds, which improved to 0.83 with the injection. Although the second fold (AUC 0.81) performed relatively well with single-energy input, it still lagged behind the full model using all energy levels. These results highlight the value of the SE-block in leveraging cross-level correlations and further validate the effectiveness of the combined approach.

In addition, prior to inject the virtual class, we optimized the parameter in the channel-wise attention mechanism—specifically, the number of output nodes in the fully connected layer following the global average pooling (GAP) in the SE-block. Due to the inherent squeezing operation, this number was constrained to be ≤ 11 (the number of channels). We conducted eleven experiments, each with a different node count, and selected 4 as the optimal value based on the highest average AUC.

comparison

III.C. Comparative Analysis with Established CNN Architectures

In clinical practice, diagnosing metastasis in breast cancer patients typically follows a two-step process: first, identifying whether the case is metastatic or non-metastatic, and second, categorizing metastatic cases as either low-burden or heavy-burden. In contrast, CNN-based methods can directly distinguish among all three classes. To further validate the effectiveness of our proposed CNN framework, we compared its performance with several widely used and well-established CNN architectures commonly applied in computer vision image recognition tasks.

tab2

Table 2: Comparison of test set AUC, parameter count, and average inference time across three folds.

Method	Parameter (million)	Time (seconds)	Test AUC - BCa 95% CI			Averaged AUC
			Fold-1	Fold-2	Fold-3	
VGG16	50.319	≈ 1.390	0.6640 [0.5470, 0.7581]	0.6553 [0.5542, 0.7520]	0.6992 [0.5935, 0.7939]	0.6728
VGG19	55.701	≈ 1.126	0.6506 [0.5389, 0.7519]	0.6387 [0.5305, 0.7471]	0.7040 [0.5984, 0.8002]	0.6644
ResNet	23.619	≈ 5.695	0.7585 [0.6484, 0.8472]	0.6833 [0.5814, 0.7773]	0.7180 [0.6209, 0.8202]	0.7199
DenseNet	7.066	≈ 12.595	0.7784 [0.6658, 0.8630]	0.7091 [0.6062, 0.8047]	0.6763 [0.5768, 0.7634]	0.7213
Proposed	0.006	≈ 0.560	0.8528 [0.7978, 0.9003]	0.8861 [0.8263, 0.9322]	0.8582 [0.8043, 0.9127]	0.8657

Table 2 compares the performance of our proposed method with several established CNN architectures, including VGG ^{simonyan2014very}, ResNet ^{he2016deep}, and DenseNet ^{huang2017densely}. The final row highlights our method, which achieved the highest average AUC of 0.8657 across three folds, demonstrating its superior effectiveness. Notably, it also required significantly fewer parameters (0.006 million) and achieved a lower average inference time (0.560 seconds), highlighting its efficiency.

III.D. ROC Curve Analysis and Statistical Validation

To provide a more detailed analysis, we compared the ROC curves of the evaluated methods. The ROC curve reflects the classification

performance of the selected model, with a shorter distance to the top-left corner (0,1) indicating better classification ability. The x-axis represents the False Positive Rate (FPR), while the y-axis denotes the True Positive Rate (TPR).

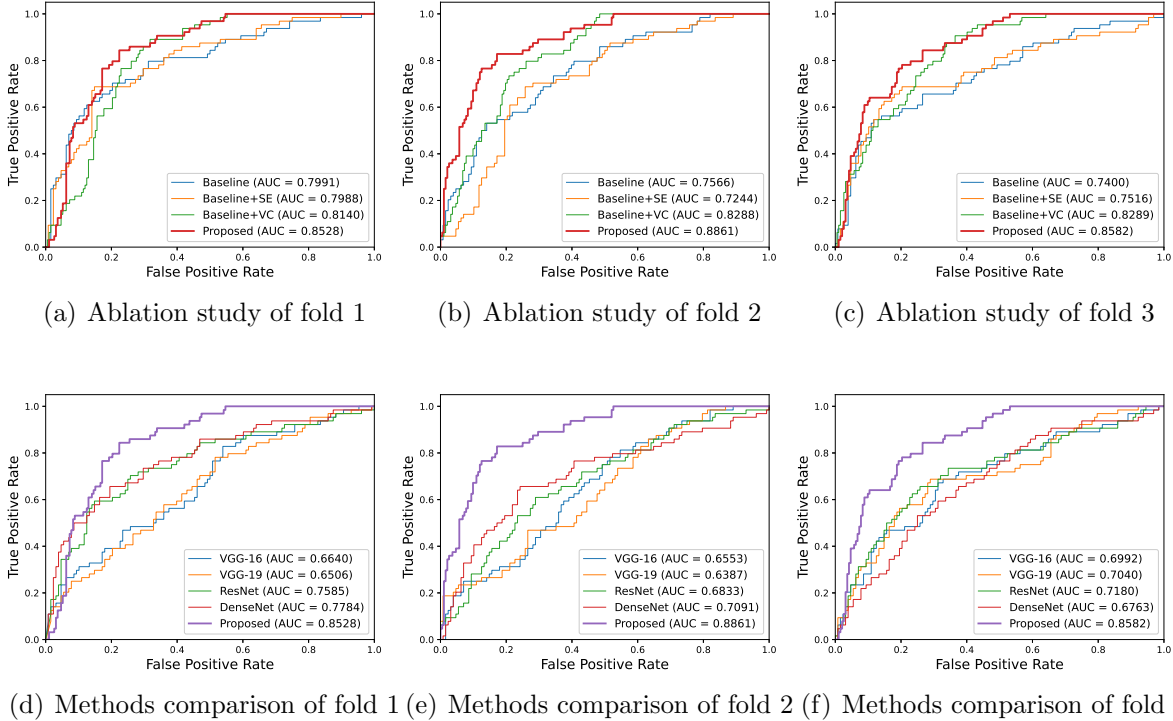


Figure 5: Subfigures (a)-(c) show the ROC curves for the three folds in the ablation study, while subfigures (d)-(f) compare the ROC curves of our proposed method with other CNN-based approaches.

Fig. 5 (a), (b), and (c) illustrate the ROC curves on the test sets for folds 1, 2, and 3, respectively, comparing the baseline model (blue line), the baseline with the SE-block (orange line), the baseline with virtual class injection (green line), and our proposed model (red line). Additionally, Fig. 5 (d), (e), and (f) present comparisons between our proposed method and other CNN-based approaches described in Subsection III.C. In these figures, our method is shown in purple, while VGG-16, VGG-19, ResNet-50, and DenseNet-121 are represented by the blue, orange, green, and red lines, respectively.

In the ROC curves from our ablation study across the three folds

(i.e., Fig. ^{curve}5 (a), (b), and (c)), all models performed above the diagonal line ($AUC = 0.5$), indicating effective classification. Both the baseline model with virtual class injection and our proposed method demonstrated strong performance ($AUC \geq 0.8$). Although both the baseline model with the virtual class and our proposed method achieved high AUC scores, their ROC curves intersected—indicating that, in some regions, the baseline model yielded higher TPR at the same FPR. To further investigate, we applied DeLong’s test ^{delong1988comparing} on the AUC values across three folds and analyzed the class-wise p-values. In fold 1, our method outperformed the baseline for classes N_0 , $N_{+(1-2)}$, and $N_{+(\geq 3)}$, with AUCs of 0.8175, 0.7109, and 0.7153, respectively, compared to 0.7986, 0.6733, and 0.6175 ($|z| > 1.96$, $p < 0.05$). In fold 2, both models performed comparably on N_0 and $N_{+(1-2)}$ ($|z| > 1.96$, $p < 0.05$), while results for $N_{+(\geq 3)}$ were not statistically significant ($|z| < 1.96$, $p = 0.053$, corrected $p = 0.1613$ after Bonferroni correction). In fold 3, our method again outperformed the baseline across all classes, achieving AUCs of 0.7718, 0.7782, and 0.7581, versus 0.6756, 0.6308, and 0.6449 ($|z| > 1.96$, $p < 0.05$).

Subfigures (d)-(f) compare our proposed method with other well-known CNN-based models across the three folds. Among all methods, only our proposed approach consistently achieved strong performance, with AUC values ≥ 0.8 , demonstrating the effectiveness of our framework. Notably, in folds 2 and 3, our proposed model consistently achieved higher TPR at the same FPR compared to the other methods.

IV. Discussion

Our previous work demonstrated the effectiveness of a CNN-based multi-class classification framework for assessing sentinel axillary lymph node metastasis in breast cancer using a special-

ized in-house dual-energy computed tomography (DECT) dataset. This pathology-confirmed dataset enables categorization into three groups: no metastasis (N_0), low metastatic burden ($N_{+(1-2)}$), and heavy metastatic burden ($N_{+(\geq 3)}$). Accurate identification of $N_{+(1-2)}$ cases may help patients avoid unnecessary axillary lymph node dissection, thereby improving clinical outcomes. Unlike existing approaches that rely on multiple data modalities—often impractical for small datasets or burdensome for radiologists—our method leverages DECT’s intrinsic spectral and spatial information. DECT enables detailed tissue characterization, making it ideal for this task. Building on our previous shallow binary classification model, which used 1×1 and 3×3 convolutions to decouple spectral and spatial features from $176 \times 176 \times 11$ tensors, we expanded the architecture to support multi-class classification, effectively addressing the first two challenges.

fig2

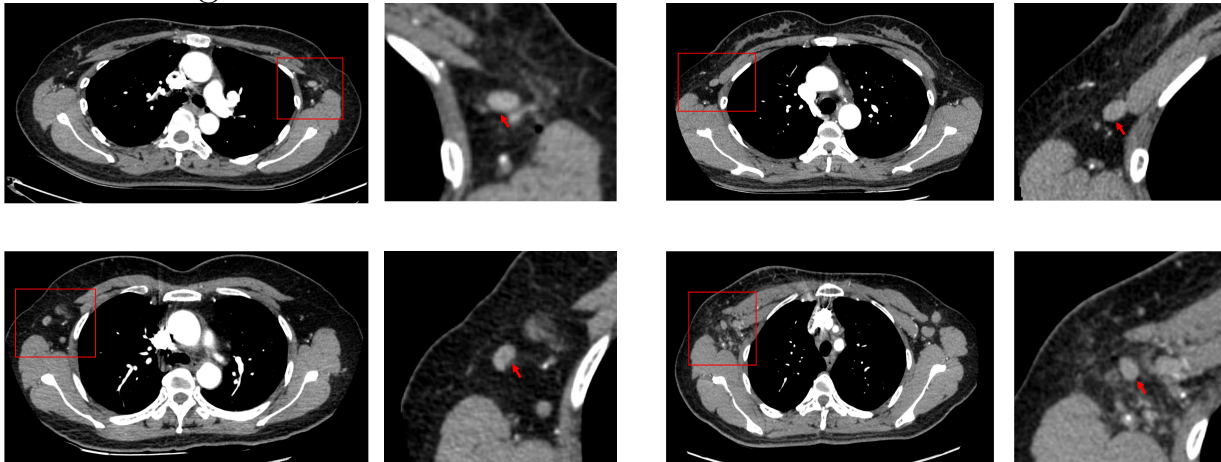


Figure 6: The first row shows patients with no metastasis N_0 and low-burden metastasis $N_{+(1-2)}$, while the second row presents cases with heavy-burden metastasis $N_{+(\geq 3)}$. Sentinel axillary lymph nodes, highlighted by red bounding box, illustrate the morphological similarities across different classes.

After addressing the initial two challenges, we further leveraged the multi-energy nature of DECT images (Fig. ^{fig1}1) and the morphological similarities among different lymph node classes (Fig. ^{fig2}6). To tackle these complexities, we focused on enhancing both the feature and representation spaces. We first introduced a feature

space-squeezing strategy, illustrated through flowcharts and formulas, which compresses information across 11 energy levels (40-140 keV, 10 keV stride). This strategy encodes and re-excites feature maps using learnable coefficients from a shallow embedding layer, improving representational capacity by refining spectral integration. To address the final challenge, we incorporated a virtual class mechanism by injecting a corresponding fake label into the representation space. Given the visual similarity across classes, this approach sharpens inter-class boundaries and compacts intra-class variations, enhancing class discrimination. It also incorporates a theoretical foundation through the formulation of a virtual softmax loss function. Together, these innovations strengthen the model's theoretical grounding and practical utility, supporting reliable clinical application in lymph node metastasis diagnosis.

Experimental results confirmed the effectiveness of our backbone design and underscored the performance gains achieved through the integration of the proposed space-squeezing strategies. Ablation studies, numerical comparisons, and ROC curve analyses demonstrated the efficiency and robustness of the overall framework. These findings strongly support the potential of our model as a reliable, non-invasive, and effective computer-aided diagnostic tool for breast cancer patients in clinical settings.

The regions of interest (RoI) in our study were limited to sentinel axillary lymph nodes, providing only localized information for breast cancer patients. Future research should broaden the scope to include additional lymph nodes, enabling a more comprehensive assessment of nodal status by fully accounting for all relevant nodes. Furthermore, developing more sophisticated models with additional perceptron layers or modules will be essential for enhancing the generalizability and robustness of the predictive framework.

V. Conclusions

This study introduces a DECT-based space-squeeze method that advances multi-class classification of metastatic lymph nodes in breast cancer. By compressing spectral-spatial features through channel-wise attention and refining representation space via virtual class injection, our approach achieves superior performance (averaged-AUC: 86.57%) in distinguishing N_0 , $N_{+(1-2)}$, and $N_{+(\geq 3)}$ categories. The method's ability to reduce diagnostic ambiguity underscores its clinical potential for guiding personalized treatment strategies, particularly in avoiding unnecessary axillary dissections for low-burden cases. Future work will expand the model's scope to include auxiliary lymph nodes and integrate advanced architectures for broader applicability. This framework establishes a robust baseline for leveraging DECT's unique

Acknowledgements

References

- ¹ H. Sung, J. Ferlay, R. L. Siegel, M. Laversanne, I. Soerjomataram, A. Jemal, and F. Bray, Global cancer statistics 2020: GLOBOCAN estimates of incidence and mortality worldwide for 36 cancers in 185 countries, *CA: a cancer journal for clinicians* **71**, 209–249 (2021).
- ² F. Bray, M. Laversanne, H. Sung, J. Ferlay, R. L. Siegel, I. Soerjomataram, and A. Jemal, Global cancer statistics 2022: GLOBOCAN estimates of incidence and mortality worldwide for 36 cancers in 185 countries, *CA: a cancer journal for clinicians* **74**, 229–263 (2024).
- ³ S. Lei, R. Zheng, S. Zhang, S. Wang, R. Chen, K. Sun, H. Zeng, J. Zhou, and W. Wei, Global patterns of breast cancer incidence

and mortality: A population-based cancer registry data analysis from 2000 to 2020, *Cancer Communications* **41**, 1183–1194 (2021).

12omission

- 4 F. Montemurro et al., Omission of axillary dissection after a positive sentinel node dissection may influence adjuvant chemotherapy indications in operable breast cancer patients, *Annals of surgical oncology* **19**, 3755–3761 (2012).

er2010ajcc

- 5 J. R. Egner, AJCC cancer staging manual, *Jama* **304**, 1726–1727 (2010).

11axillary

- 6 A. E. Giuliano, K. K. Hunt, K. V. Ballman, P. D. Beitsch, P. W. Whitworth, P. W. Blumencranz, A. M. Leitch, S. Saha, L. M. McCall, and M. Morrow, Axillary dissection vs no axillary dissection in women with invasive breast cancer and sentinel node metastasis: a randomized clinical trial, *Jama* **305**, 569–575 (2011).

t2017eight

- 7 Á. Sávolt, G. Péley, C. Polgár, N. Udvarhelyi, G. Rubovszky, E. Kovács, B. Győrffy, M. Kásler, and Z. Mátrai, Eight-year follow up result of the OTOASOR trial: the optimal treatment of the axilla—surgery or radiotherapy after positive sentinel lymph node biopsy in early-stage breast cancer: a randomized, single centre, phase III, non-inferiority trial, *European Journal of Surgical Oncology (EJSO)* **43**, 672–679 (2017).

2022breast

- 8 W. J. Gradishar et al., Breast cancer, version 3.2022, NCCN clinical practice guidelines in oncology, *Journal of the National Comprehensive Cancer Network* **20**, 691–722 (2022).

ouk2017pre

- 9 J. H. Youk, E. J. Son, J.-A. Kim, and H. M. Gweon, Pre-operative evaluation of axillary lymph node status in patients with suspected breast cancer using shear wave elastography, *Ultrasound in medicine & biology* **43**, 1581–1586 (2017).

- predicting¹⁰ G. Tapia, V. Ying, A. D. Re, A. Stellin, T. Y. Cai, and S. Warrior, Predicting non-sentinel lymph node metastasis in Australian breast cancer patients: are the nomograms still useful in the post-Z0011 era?, *ANZ journal of surgery* **89**, 712–717 (2019).
- 3axillary¹¹ J. S. Ecanow, H. Abe, G. M. Newstead, D. B. Ecanow, and J. M. Jeske, Axillary staging of breast cancer: what the radiologist should know, *Radiographics* **33**, 1589–1612 (2013).
- 8axillary¹² X. Zhang, C. Zheng, Z. Yang, Z. Cheng, H. Deng, M. Chen, X. Duan, J. Mao, and J. Shen, Axillary sentinel lymph nodes in breast cancer: quantitative evaluation at dual-energy CT, *Radiology* **289**, 337–346 (2018).
- 2020lymph¹³ L.-Q. Zhou et al., Lymph node metastasis prediction from primary breast cancer US images using deep learning, *Radiology* **294**, 19–28 (2020).
- s2014does¹⁴ A. Evans, P. Rauchhaus, P. Whelehan, K. Thomson, C. A. Purdie, L. B. Jordan, C. O. Michie, A. Thompson, and S. Vinnicombe, Does shear wave ultrasound independently predict axillary lymph node metastasis in women with invasive breast cancer?, *Breast cancer research and treatment* **143**, 153–157 (2014).
- y2010cost¹⁵ J. C. Boughey, J. P. Moriarty, A. C. Degnim, M. S. Gregg, J. S. Egginton, and K. H. Long, Cost modeling of preoperative axillary ultrasound and fine-needle aspiration to guide surgery for invasive breast cancer, *Annals of surgical oncology* **17**, 953–958 (2010).
- 6nomogram¹⁶ S.-Q. Qiu, H.-C. Zeng, F. Zhang, C. Chen, W.-H. Huang, R. G. Pleijhuis, J.-D. Wu, G. M. van Dam, and G.-J. Zhang, A nomogram to predict the probability of axillary lymph node metastasis in early breast cancer patients with positive axillary ultrasound, *Scientific reports* **6**, 21196 (2016).

- la2016role¹⁷ N. La Verde et al., Role of patient and tumor characteristics in sentinel lymph node metastasis in patients with luminal early breast cancer: an observational study, *Springerplus* **5**, 1–9 (2016).
- predicting¹⁸ G. Tapia, V. Ying, A. Di Re, A. Stellin, T. Y. Cai, and S. Warrior, Predicting non-sentinel lymph node metastasis in Australian breast cancer patients: are the nomograms still useful in the post-Z0011 era?, *ANZ Journal of Surgery* **89**, 712–717 (2019).
- decoupling¹⁹ R. Zeng, X. Zhang, C. Zheng, J.-H. Du, Z. Gao, W. Jun, J. Shen, and Y. Lu, Decoupling convolution network for characterizing the metastatic lymph nodes of breast cancer patients, *Medical Physics* **48**, 3679–3690 (2021).
- 1987better²⁰ B. Efron, Better bootstrap confidence intervals, *Journal of the American statistical Association* **82**, 171–185 (1987).
- 018virtual²¹ B. Chen, W. Deng, and H. Shen, Virtual class enhanced discriminative embedding learning, *Advances in Neural Information Processing Systems* **31** (2018).
- an2014very²² K. Simonyan and A. Zisserman, Very deep convolutional networks for large-scale image recognition, *arXiv preprint arXiv:1409.1556* (2014).
- he2016deep²³ K. He, X. Zhang, S. Ren, and J. Sun, Deep residual learning for image recognition, in *Proceedings of the IEEE conference on computer vision and pattern recognition*, pages 770–778, 2016.
- 017densely²⁴ G. Huang, Z. Liu, L. Van Der Maaten, and K. Q. Weinberger, Densely connected convolutional networks, in *Proceedings of the IEEE conference on computer vision and pattern recognition*, pages 4700–4708, 2017.
- 8comparing²⁵ E. R. DeLong, D. M. DeLong, and D. L. Clarke-Pearson, Comparing the areas under two or more correlated receiver operating

characteristic curves: a nonparametric approach, *Biometrics* , 837–845 (1988).